Print geometry alterations and layer staggering to enhance the mechanical properties of plain and fiber-reinforced 3D printed concrete

Avinaya Tripathi[*], Sooraj A.O. Nair[*], Harshitsinh Chauhan[*], Narayanan Neithalath[†]

Abstract

Conventional approaches to concrete 3D printing relies on printing concrete in a straight (linear) print path, with layers overlaid on top of each other. This results in inter-layer and inter-filament joints being potential weak spots that compromise the mechanical performance. This paper evaluates simple alterations to the print geometry to mitigate some of these effects. A printable mixture with 30% of limestone powder replacing cement (by mass), with a 28-day compressive strength of about 70 MPa in the dominant direction, is used. S- and 3-shaped print paths are evaluated as alternatives to the linear print path, which are found to result in strength enhancement. Staggering of the layers ensures that the inter-filament joints do not lie on the same plane along the depth. Flexural strength enhancements of 10-30% are observed when the print geometries are changed and/or layers are staggered. The differences in compressive strengths between mixtures printed with different layouts or configurations are not very significant, unlike in the case for flexure. The study shows that modifications in print geometry (shapes and orientation) can be used to mitigate mechanical property reductions attributed to inter-filament defects in layered 3D printing.

Keywords: 3D printing; orientation; layer geometry; anisotropy; strength

[*] Graduate student, School of Sustainable Engineering and Built Environment, Arizona State University, Tempe AZ 85287

[†] Professor, School of Sustainable Engineering and Built Environment, Arizona State University, Tempe AZ 85287; Corresponding author: e-mail: Narayanan.Neithalath@asu.edu

1. Introduction

3D concrete printing is attracting a lot of interest in the construction industry because of its numerous advantages like freedom to create complex architectures, optimized material use, ability to print on-demand structures, and reduced labor requirement [1]–[5]. This has resulted in concurrent advances in novel materials that satisfy stringent rheology and strength development requirements, and printing systems capable of executing complex geometries in an efficient manner. However, several challenges from a materials standpoint still exist. The combined attainment of pumpability, extrudability and buildability, which sometimes necessitates contradictory material properties, is still a challenge. However, through careful material design, admixtures for rheology control, and print path planning, efforts are ongoing to address these impediments [6]–[10]. While attention has rightly been focused on rheology and consequent printability of concrete, mechanical properties of 3D printed concrete has been treated for most part, like those of conventional concrete, except for allowances for the layered construction method that induces anisotropy in properties. It has been reported that the mechanical properties of 3D printed concrete structures can likely be inferior to those fabricated using traditional casting techniques [10]–[12].

Since the 3D printing process involves laying individual filaments side-by-side and stacking layers of filaments one over the other, there are several likely zones of weakness in the overall structure, which results in reduced mechanical performance [13]–[17]. Compressive strengths of 3D printed specimens are generally reported for the three orthogonal directions [11], [18], [19]. The direction of maximum strength is dependent on the method of casting and the process aspects involved in 3D printing, including the nozzle standoff distance, which makes generalizing the results rather difficult. While higher strengths can be achieved through changes in material design [20], [21], the effects of planes of weakness that are introduced through layering cannot be overcome using improved materials alone. It is in this context that there is a need to investigate the arrangement of inter-filamentous and inter-layer joints that results in different levels of anisotropy in a 3D printed structural element. Changing the direction of printing of individual filaments within a layer, or layers within a component will change the direction-dependent mechanical properties, thereby providing an option to optimize the desired performance.

For instance, filaments of rectangular cross-section (with or without bull-nosed edges) are printed in straight lines (unless it is an architectural structure with a non-linear geometry) and subsequent layers are overlaid symmetrically on top of the lower layers. This results in the inter-filamentous joints in each layer aligning along the entire depth of the structure. When tested in flexure, if there is only one filament width that is tested, this effect will not be captured, but when samples with multiple filaments are tested, this effect will dominate. Instead of printing the filaments in a straight path, curving of the print paths in a prismatic specimen will result in non-alignment of regions of weakness along the direction of loading, thereby likely enhancing

the strength. This aspect is evaluated in this work. Furthermore, based on the nozzle type used (circular or rectangular), the extent of discontinuity at locations where the filaments meet in the horizontal and vertical directions can result in reduced mechanical performance. A potential work around is to stagger the filaments in each layer so that the inter-filamentous joints do not occur in different layers exactly above one another. This aspect is also explored in this paper. In addition to linear or straight filament printing, this paper explores S-shaped and 3-shaped printing paths to evaluate their influence on the flexural performance when the layers perpendicular to the direction of loading, and cube compressive strengths in the three orthogonal directions. The synergistic effects of fiber reinforcement – either steel or basalt, along with the aforementioned geometric modifications, are also studied in this paper.

2. Experimental Program

2.1. Material and mixtures

The mortar mixtures in this study were proportioned using Type I/II ordinary portland cement (OPC) conforming to ASTM C150, fine limestone (L) powder conforming to ASTM C568, and commercial sand (M), having a median particle size of 0.20 mm, conforming to ASTM C778. The chemical and physical properties of the mortar components are provided in Table 1 and their particle size distributions (PSD) in Figure 1. Chopped steel fibers (SF) and chopped basalt fibers (BF), the properties of which are shown in Table 2, were used as fiber reinforcement. A polycarboxylate ether-based superplasticizer (at a dosage of 0.20%-0.35% by mass of the binder) was used in all the mixtures. The mortar mixture proportions shown in Table 3 were derived from authors' earlier work that considered particle packing and rheological characteristics that are necessary for printability (i.e., extrudability and buildability) [22]. The selected mortar mixture (L_{30}; containing 30% of fine limestone powder by mass as cement replacement) has also been used by the authors to evaluate the influence of different layer heights on the compressive, flexural and fracture response of 3D printed specimens [23]. All mixtures contained 50% sand by mass of the total solids in the mortar, as shown in Table 3.

Table 1: Chemical composition and physical properties of the mortar components.

Components of the binders	Chemical composition (% by mass)							d_{50} (μm)	Specific gravity
	SiO_2	Al_2O_3	Fe_2O_3	CaO	MgO	SO_3	LOI*		
OPC	19.60	4.09	3.39	63.21	3.37	3.17	2.54	10.4	3.15
Limestone(L)	$CaCO_3$>99%							1.5	2.70
Medium Sand (M)	SiO_2>99%							200	2.40
*Loss of Ignition									

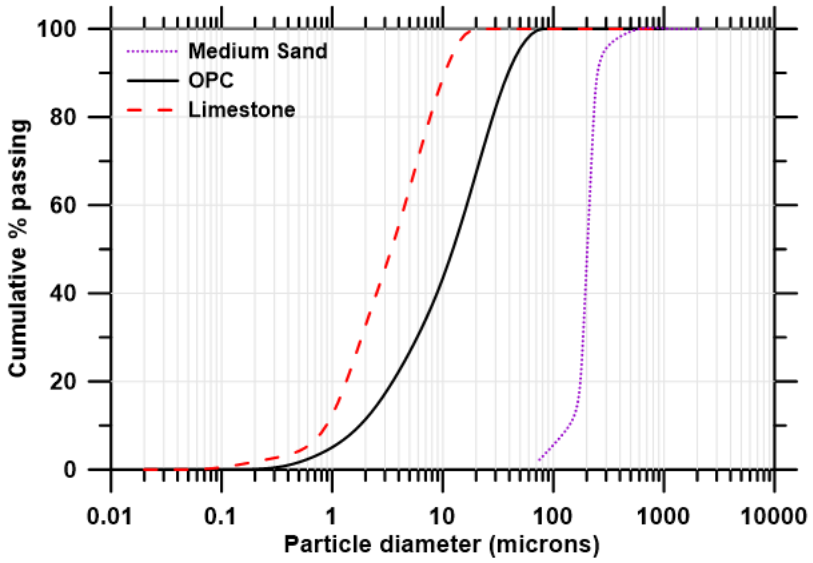

Figure 1: Particle size distribution of the mortar components.

Table 2: Properties of the fibers used in the study.

Type of Fibers	Diameter (mm)	Length (mm)	Specific gravity	Tensile Strength (GPa)	Young's Modulus (GPa)
Chopped Steel Fiber (SF)	0.20	13	6.80	3.0	210
Chopped Basalt Fiber (BF)	0.04-0.06	15	2.36	0.28	18

Table 3: Mortar mixture proportions used in the study.

Mixture ID	Mass Fraction of Ingredients			Chopped Steel Fiber (SF)[+]	Chopped Basalt Fiber (BF)[+]	Water-to-binder ratio (w/b) by mass	SP to binder ratio (SP%) by mass of the binder
	OPC	Limestone (L)	Sand (M)				
L_{30}	0.35	0.15	0.5	-	-	0.35	0.25
$L_{30\text{- SF}}$	0.35	0.15	0.5	0.28	-	0.35	0.35
$L_{30\text{- BF}}$	0.35	0.15	0.5	-	0.28	0.35	0.35
[+]Percentage by volume of the mixture.							

2.2. 3D printing of mortars

A gantry-based 3D printer equipped with a screw extrusion system (shown in Figure 2) was used to print the selected mortars shown in Table 3. To obtain consistent filament cross-section dimensions (i.e., invariant layer widths for non-orthogonal prints), a circular nozzle of diameter (ND) 20 mm was used instead of a rectangular nozzle. Mortar slabs of size 400 × 400 × 60 mm were printed at an in-plane print speed of 50 mm/s. To obtain uniform filaments of layer height (LH) 10 mm (0.5 × ND) and layer width (LW) of 20 mm (equal to ND), the stepper for the screw extruder was calibrated for a flow rate of about 10 ml/s. A layer height of 10 mm was selected based on authors' previous work [23] which showed that lower LH is beneficial for plain mixtures

since a non-zero standoff distance, resulting in some consolidation, will mitigate the likely adverse effects of layer interfaces. For fiber-reinforced mixtures designed using stiff fibers such as chopped steel fibers, a LH that is at least equal to or greater than the fiber length is preferable, as otherwise the defects due to scratching of fibers and fibers not being totally confined in layers become significant [23].

The print filament layouts (note that these are the plan geometries; the cross section always remains rectangular) chosen for this study were straight line (or linear), S-shaped, and 3-shaped. Detailed description of the dimensions for different filament types are provided in Figure 3. S-shaped and 3-shaped filaments consist of arcs of chord length 100 mm formed on a circle of radius 120 mm laid side-by-side. For the S-shaped prints, the arc alternates between convex and concave (i.e., changes direction alternatively), while for the 3-shaped prints, the arcs are in the same direction (i.e., always convex), as shown in Figure 3. These three chosen filament layouts (linear, S-shaped, and 3-shaped) were printed in two different ways - first, conventional printing, where filaments of the new layer were laid exactly above the corresponding filament on the lower layer, and second, staggered printing, where filaments of the new layer were staggered by half the layer width. Three-dimensional representations of the conventional (C) and staggered (S) printing types, for linear, S-shaped, and 3-shaped prints are shown in Figure 4. The letters 'C' or 'S' following the print geometry type – linear (L), S-shaped (S), or 3-shaped (3), indicate the configuration. Note that the 3-shaped filament printing was only done for the conventional arrangement and not for the staggered one as 3-shaped print demonstrated reduced mechanical performance than the S-shaped print in preliminary studies. Moreover, the S-shaped prints were found to be more effective in enabling a smoother printing, because of the easy transition between the convex and concave arcs, as opposed to transition from one convex to another convex arc. Slabs were 3D printed (see Figure 5), and moist-cured in a curing chamber, at 23±2^{o}C and >98% RH, for 28 days. After the curing duration, they were cut into cubes and beams (as shown in Figure 6) for compression and flexural tests.

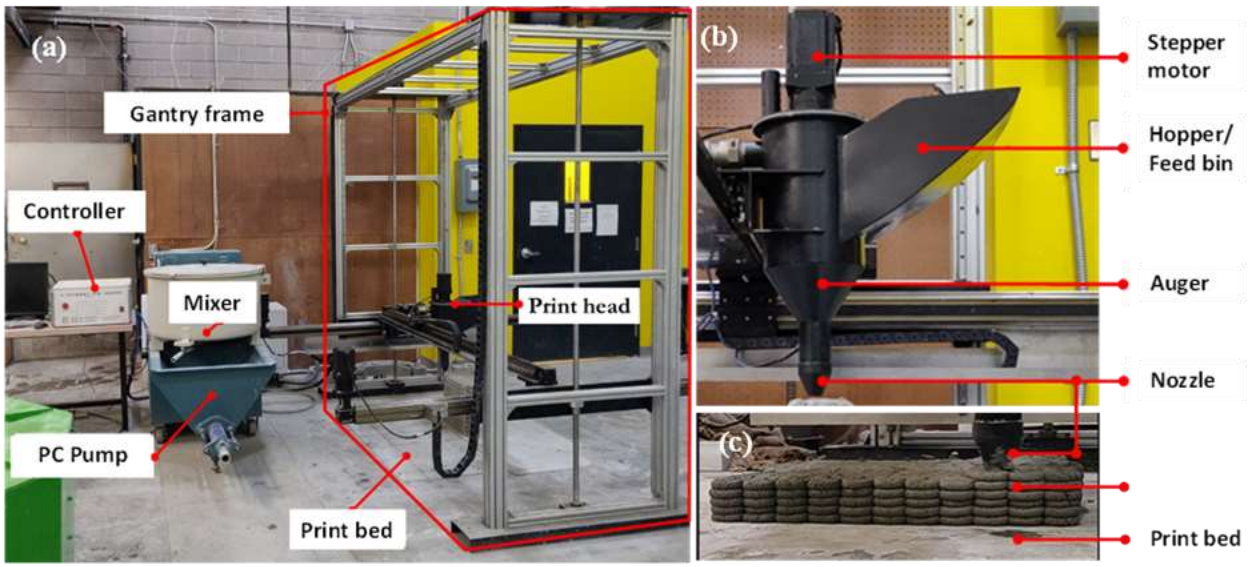

Figure 2: Printer setup showing: (a) the gantry printer with the controller and the mixer, (b) close-up of the print head, and (c) S-shaped conventional (S-C) print in progress.

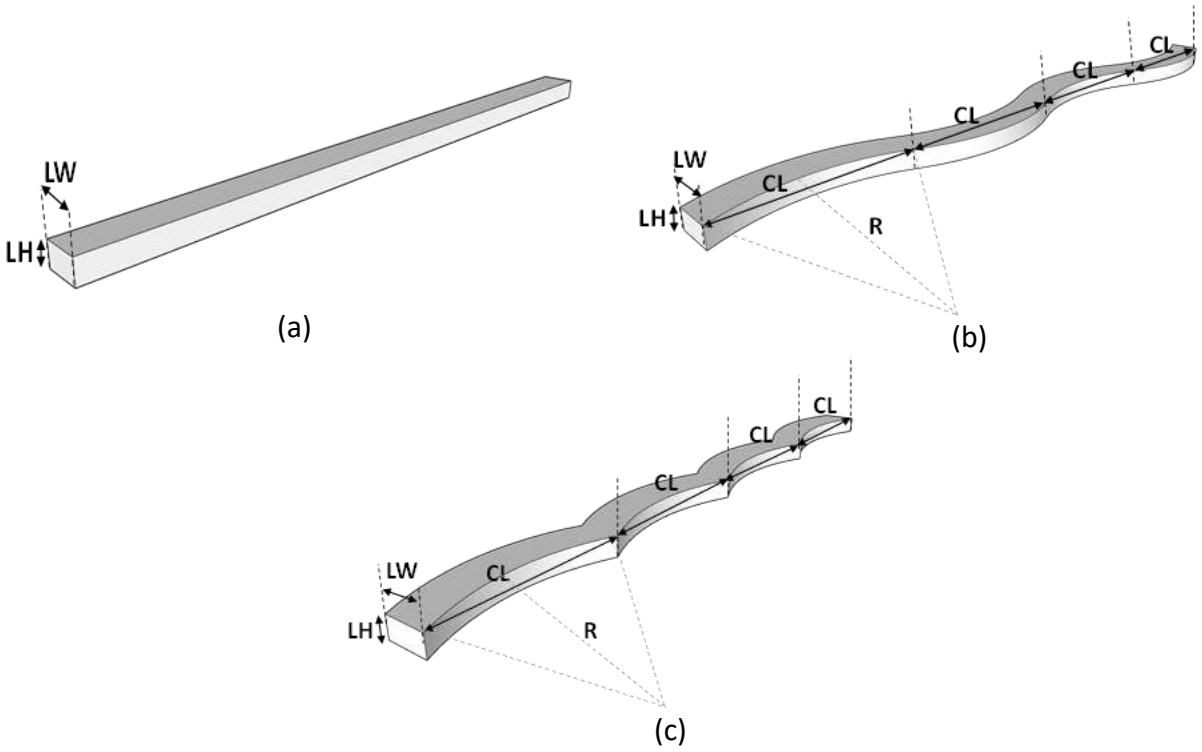

Figure 3: Filament geometries used in this study: (a) linear (L), (b) S-shaped (S), and (c) 3-shaped (3). The layer height (LH) used was 10 mm, the layer width (LW) was 20 mm, the chord length (CL) was 100 mm, and the radius of arc (R) was 120 mm.

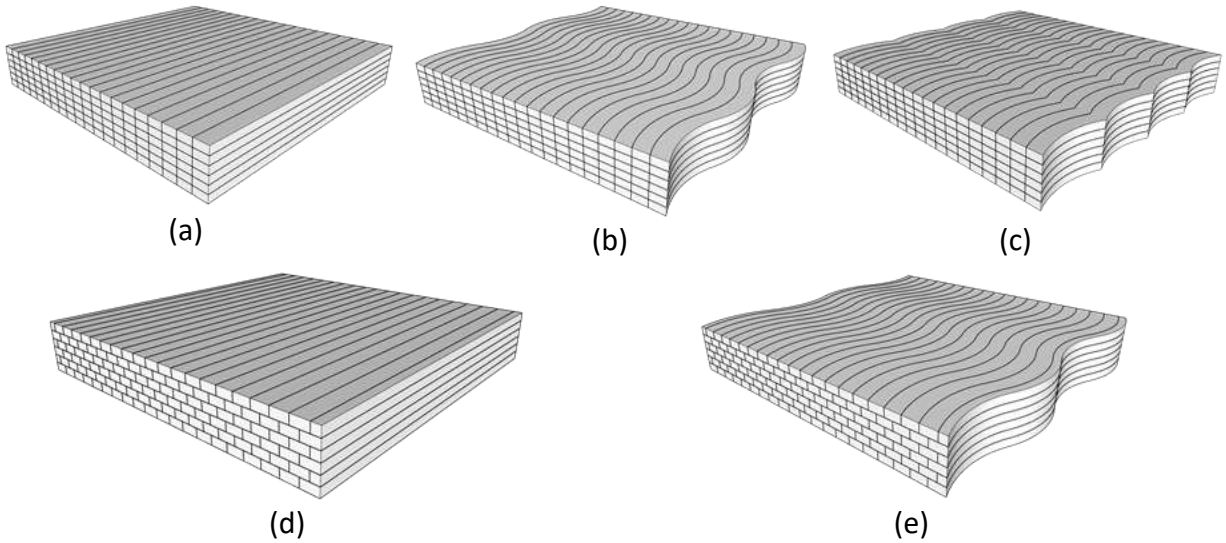

Figure 4: Three-dimensional representation of printed slabs using different geometries of filaments and their configurations: (a) linear conventional (L-C), (b) S-shaped conventional (S-C), (c) 3-shaped conventional (3-C), (d) linear staggered (L-S), and (e) S-shaped staggered (S-S). Note that in the nomenclature use, the first letter/number indicates the filament geometry (linear, S-shaped, or 3-Shaped), and the second letter indicates the configuration in which it is printed (conventional or staggered).

Figure 5: Printed slab (a) linear conventional (L-C), (b) S-shaped staggered (S-S), and (c) 3-shaped conventional (3-C).

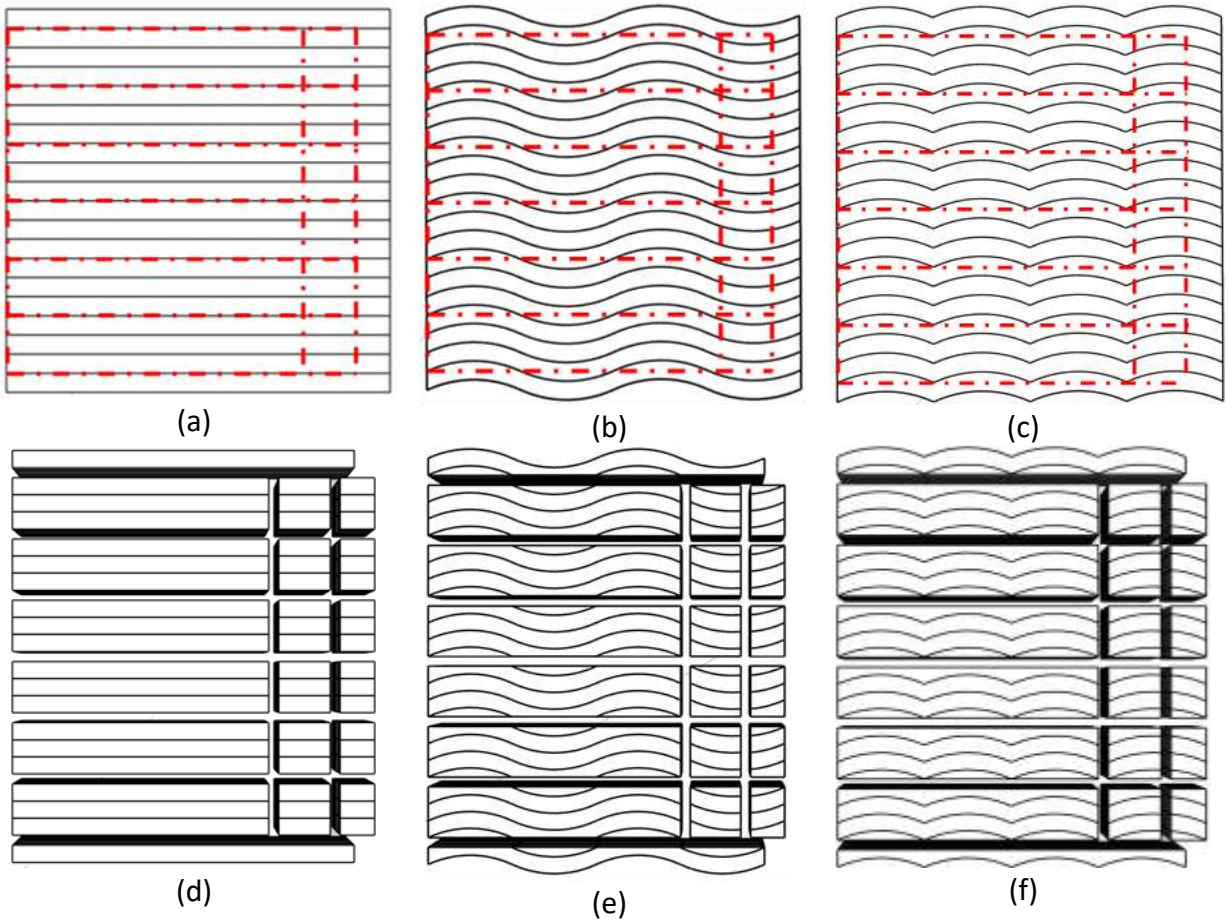

2.3. Figure 6: Top view of (a) R-C, (b) S-C, and (c) 3-C slabs with dotted lines showing the region of cut to obtain beams and cubes shown in (d), (e) and (f) respectively. Flexural testing

After 28 days of moist curing, the 3D printed slabs were cut into beams (60 × 60 × 300 mm in size) such that the filament print direction is oriented parallel to the longer side of the beam. One of the longer 300 mm faces perpendicular to the filament direction was speckled with black paint to enable the use of digital image correlation (DIC) to track surface displacements and crack initiation and propagation. Flexural response of the beams was obtained in accordance with ASTM C78/C78M-18 [24] under four-point bending. A servo-controlled universal testing machine (MTS 810) with a capacity of 100 kN was used. The test was carried out under mid-point deflection control using LVDTs, at a rate of 0.02 mm/min until either failure occurred or the load capacity dropped to 500 N, or the total deflection at center of the beam reached 0.8 mm, whichever happened first. Figure (a) shows the general test setup and the corresponding components.

2.4. Compression testing

Cubes of 60 × 60 × 60 mm (shown in Figure (a)) were prepared by cutting the slab. These cubes were then subjected to uniaxial compression using a servo-controlled universal testing machine (SBEL CT-110-S) with a maximum capacity of 489 kN. Compression tests were carried out in all

three orthogonal directions for the different print layouts and configurations. Direction-1 represents the case where load is applied along the X-axis (perpendicular to the faces lying in Y-Z plane, where printing happens along the X-direction), Direction-2 along the Z-axis (perpendicular to the faces lying in X-Y plane) and Direction-3 along the Y-axis (perpendicular to the faces lying in X-Z plane), as shown in Figure (b)-(d). Loading was done at a stroke displacement rate of 0.15 mm/min corresponding to an initial strain rate of 0.25%/min. The test setup is shown in Figure (b).

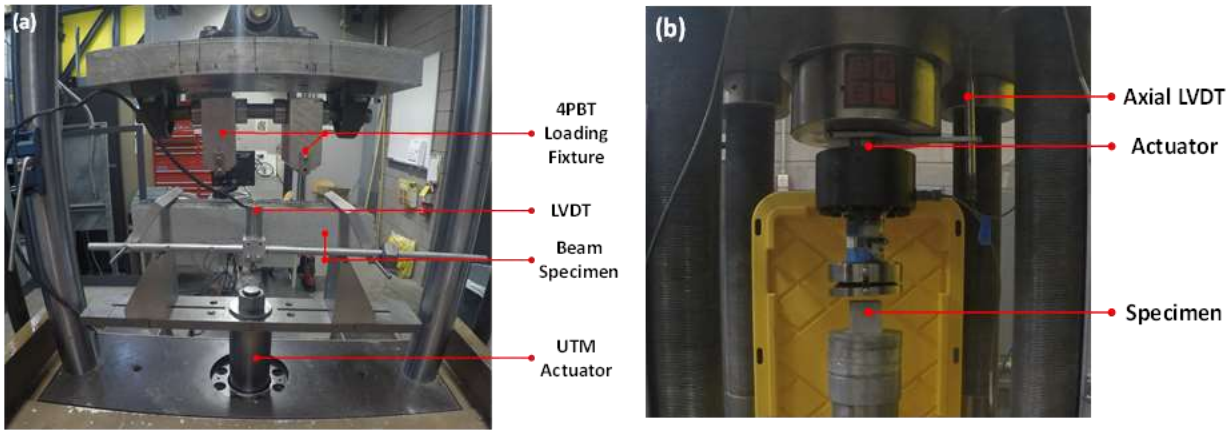

Figure 7: (a) Flexure test setup, and (b) uniaxial compression test setup; showing different components.

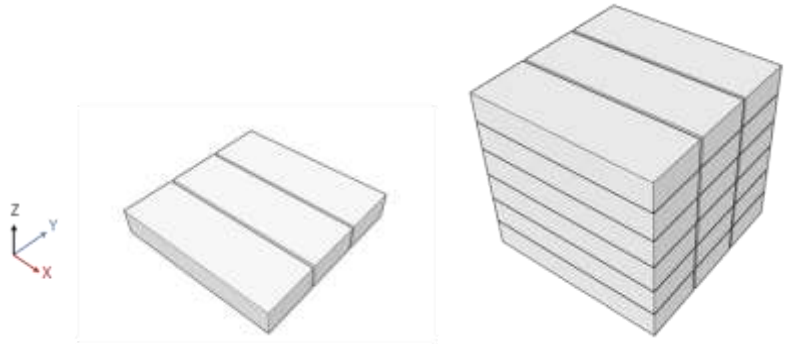

(a)

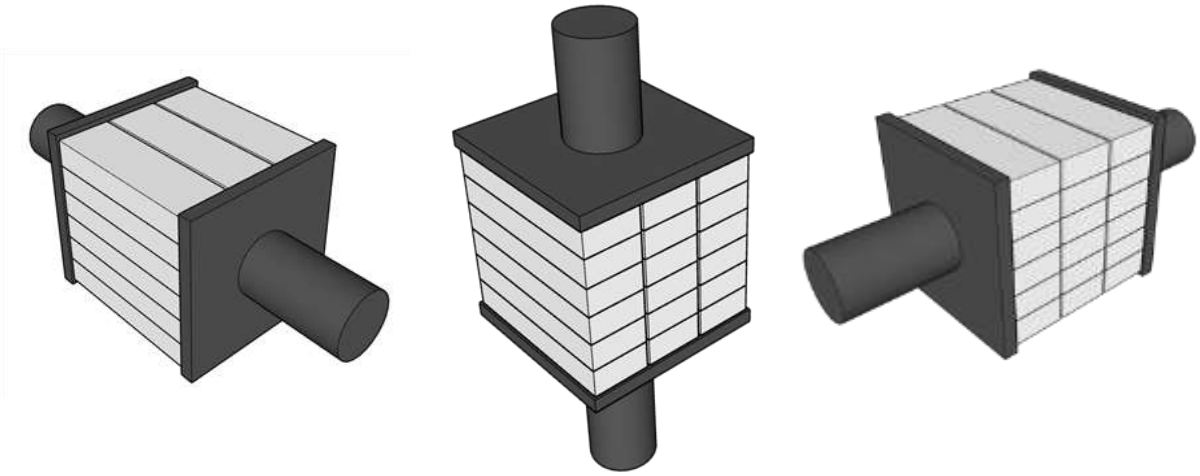

(b) (c) (d)

Figure 8: (a) Representative single layer and complete cube showing 3 filaments and 6 layers; the print direction is parallel to X-axis; and compression testing along (b) Direction-1, (c) Direction-2, and (d) Direction-3.

2.5. Digital image correlation for visualizing strain fields and crack propagation

Digital image correlation (DIC) is used as a non-contact means to acquire the surface displacements and strain fields in the specimens during the flexural testing. Strain profiles extracted from the DIC data is used to identify and track crack initiation and propagation, and to extract the true displacement (deflection at the mid-point) of the specimen. The DIC setup shown in Figure 7(a) consists of two cameras focused on a speckled area of interest on the beam, which is illuminated by high-intensity flood lights. The data acquisition (DAQ) unit controls the cameras. The frequency of image capture is fixed at 1 Hz. The mid-point deflection of beam extracted from the DIC analysis is also compared to the deflection obtained from the LVDT in the closed-loop test setup. Figure 7(b) shows a typical Lagrangian strain field in the beam subjected to four-point bending. The process of obtaining Lagrangian strain fields from the displacement field captured by DIC is described in detail elsewhere [25], [26].

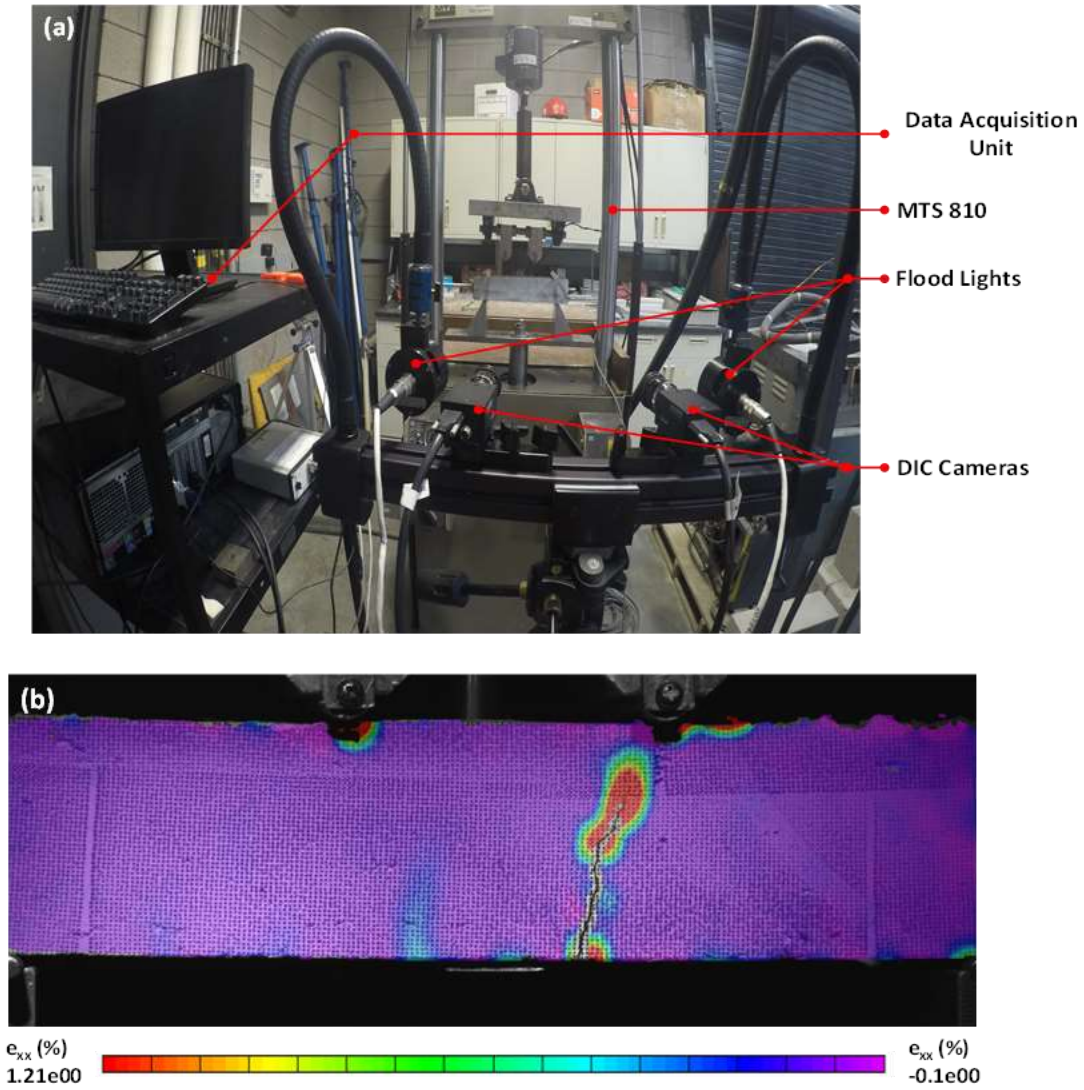

Figure 7: (a) DIC setup, and (b) representative Lagrangian strain field (just before end of test in a S-S-SF beam) subjected to four-point bending.

3. Results and Discussions

3.1. Flexural response of the beams with different layer patterns and configurations

3.1.1. Effect of filament print layout and configuration on flexural strength of unreinforced specimens

As discussed earlier, three different print layouts were used in this work. The effect of print layout (linear (L), S-shaped(S), and 3-shaped(3)) on the flexural strengths of the conventionally laid (not staggered) unreinforced 3D printed beams (denoted as L-C, S-C, and 3-C) are reported first. The flexural specimens (60 × 60 × 300 mm) were tested such that the filaments were oriented along the length direction. The span length used for testing was 240 mm. The average flexural strengths for beams printed using L-, S-, and 3-shaped geometries are shown in Figure 8(a). It is clearly

noticed that by changing the individual filament print layout (plan geometry), flexural strengths of the printed beams can be enhanced. Among the three layouts, the S-shaped layout (S-C) gives the highest average flexural strength, which is about 15% higher than that of the regular linear geometry (L-C), which is the most common print (plan) geometry. The use of a 3-shaped printing layout also increases the flexural strength by about 10% or more compared to the L-C case. The enhancements in flexural strength can be explained based on the nature of inter-filament joints present in 3D-printed elements. Inter-filament joints are the joints present between two adjacent filaments in the plan view (as opposed to inter-layer joints which are present between the adjacent layers in the cross-sectional view). The 3D printing process and the nozzle standoff distance used typically results in some amount of layer consolidation, resulting in densification of the inter-layer joints, while the inter-filament joints do not benefit from such consolidation, and are generally weaker [15]–[17]. In a beam conventionally printed using straight filaments (L-C), the weaker inter-filament joints run parallel to the length direction, while in the S-C and 3-C print layouts, the inter-filament joints are curved (see Figure 6(d)-(f)), creating more contact area between the filaments for the same length of the beam (300 mm). Moreover, the curved paths also ensure that the stress required to separate the adjacent filaments is higher since the inter-filament contact path is more tortuous. It is possible to note from the S-C and 3-C geometries (shown in Figure 3, Figure 4(a)-(c), and Figure 6) that the 3-C geometry induces more inter-filament stress concentrations than the S-C geometry because of the sharp changes in path needed to keep the arcs convex always, thereby resulting in slightly lower strengths. However, the flexural strengths are still higher than that of the conventional case. The results shown here indicate that it is possible to alter the print plan layout, while maintaining the other parameters the same, to obtain higher flexural strengths. In the forthcoming sections of the paper, the comparisons are restricted to the straight linear (L) and S-shaped print layouts. Even though the 3-shaped prints showed better strengths than the linear prints, it was observed that S-shaped prints enable smoother printing, and consequently lesser defects, the reasons for which were explained earlier.

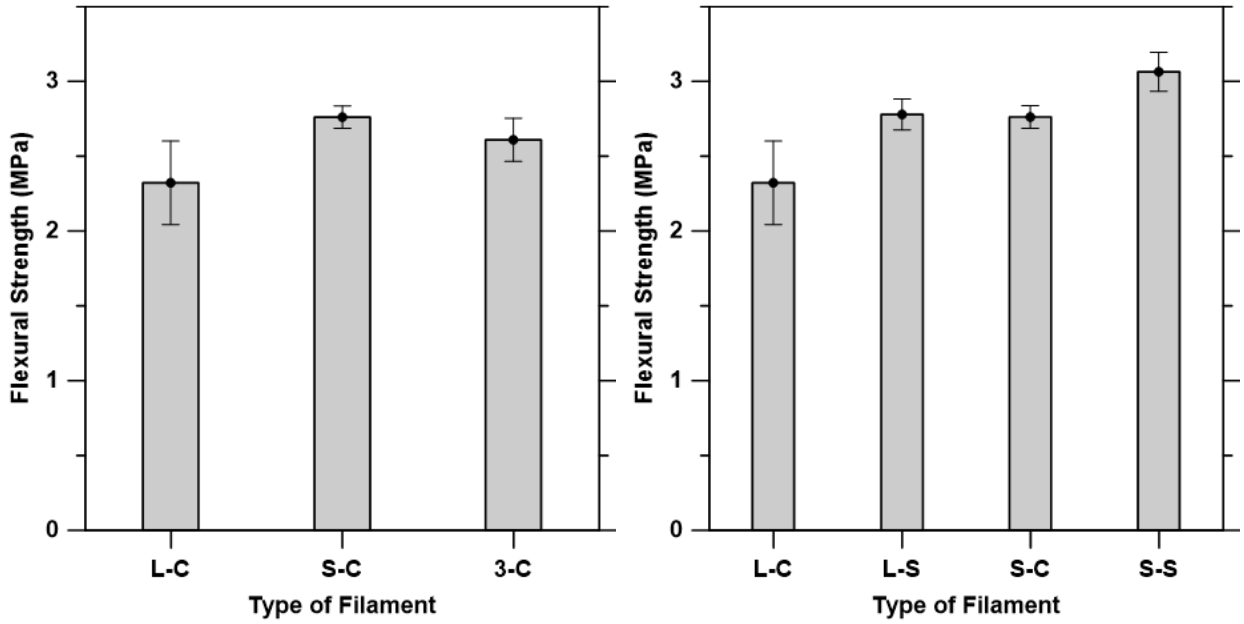

Figure 8: Flexural strengths of beams printed using different layouts: (a) L-C, S-C, and 3-C; and (b) L-C, L-S, S-C and S-S geometries. All the beams were subjected to four-point bending test. The error bars correspond to standard deviation from three or more replicate specimens.

It was observed in our previous work [23] that, despite adjusting the flow rate and print speed to reduce the chances of formation of inter-filament voids, this was not always feasible. To mitigate this concern to a certain extent, staggered printing configuration is adopted in this work where the filaments in the upper layer are staggered by half a layer width in the plane of printing. Figure 8(b) shows the flexural strengths of the staggered L and S prints along with those of their non-staggered (conventional) counterparts. Staggering the layers in an S-shaped print geometry (S-S) results in an increase in flexural strength of about 25% as compared to the conventional linear mode of printing that is commonly adopted (L-C), and more than 10% as compared to the linear layout in the staggered configuration (L-S). Changing the print configuration from conventional to staggered results in inter-filament defects not lining up perfectly – in other words, some tortuosity in the crack path that likely follows the inter-filament contacts is introduced, which helps enhance the load carrying capacity. When compared to its non-staggered counterpart (S-C), the strength enhancement is seen to be about 10%. The flexural strength results reported here shows that it is indeed beneficial to consider alternate printing layouts (in plan geometry) and layer configurations to mitigate the mechanical property reduction associated with some of the common defects encountered in concrete 3D printing.

3.1.2. Effect of fiber reinforcement

Since the staggered print configuration performed better than the conventional print configuration (as shown in Figure 8), the influence of fiber reinforcement is evaluated here only for the staggered print configuration. It is shown in many recent publications that fibers (metallic or polymeric) added to a 3D printed matrix helps in crack control and/or enhances the strength and toughness, based on the fiber type [27], [28]. Figure 9 shows the flexural strengths of

mixtures reinforced with either steel or basalt fibers, and the comparison with unreinforced mixtures printed with different filament layouts. Note that both basalt and steel fibers have similar lengths, but the basalt fibers have significantly smaller diameters. The volume fractions of the fibers used are the same for both fiber types (0.28% by volume of the mortar). The flexural strength results indicate clear enhancement in flexural strengths due to fiber incorporation, which is expected. An increase in flexural strength by about 10-30% is noted when either of the two types of fibers are incorporated into the specimens printed in the L and S-shaped layouts, with a more noticeable enhancement for the staggered linear (L-S) print type. The reason for reduced efficiency of fibers in the S-shaped mixtures, especially for stiff fibers, is that the print direction changes in a wavy pattern, and the fibers cannot consistently be oriented in the print direction. Moreover, for the linear geometry, as explained earlier, the inter-filament defects are more, which the enhanced capacity through the use of fibers overcomes to a certain extent. Thus, fibers, which orient along the direction of print are seen to benefit the linear print geometry better [29]–[32].

For both the linear and S-shaped filament layouts, the basalt fiber reinforced mixture is observed to slightly outperform the steel fiber reinforced mixture from a flexural strength standpoint. As was shown in our previous work [23], stiffer steel fibers, when introduced in a layer that has a lower layer height than the fiber length, results in scratching of the surface of the layer during the printing process. This causes surface defects that lead to the total effect of fibers not being realized with respect to flexural strength. This shows that less stiff fibers such as basalt fibers (E lower by an order of magnitude as compared to steel fibers; see Table 2) could be used to obtain enhanced flexural strengths in 3D printed concrete elements. More importantly, a lower layer height (than the fiber length) can be used, since it has been shown that a lower layer height is beneficial in enhanced mechanical performance [23], even though the speed of construction could somewhat be compromised. It also needs to be recognized that, for a given volume fraction of fibers, there are about 13 times the number of basalt fibers in the mixture as compared to steel fibers, based on their diameter difference. More number of fibers in a unit volume enables the matrix to efficiently transfer stresses. Higher fiber density in the matrix also enhances the crack path tortuosity, which extends the load carrying capacity in this case. While a layered printing process will always encounter issues related to inter-layer and inter-filament strength, the aforementioned discussions demonstrate that geometric modifications, along with material modifications (such as the use of fiber reinforcement) can be suitably used to mitigate some of these effects from a viewpoint of flexural strength.

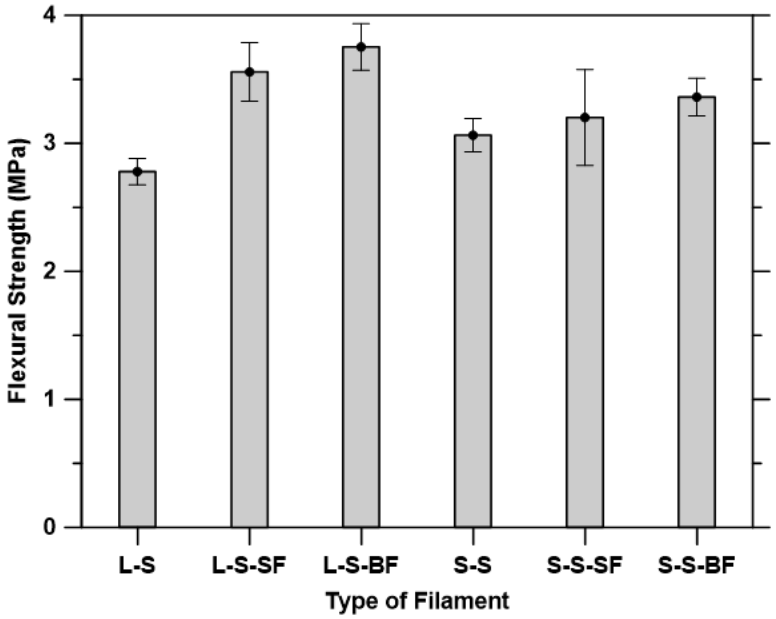

Figure 9: Flexural strength of beams with different layout-configuration combinations (L-S, L-S-SF, L-S-BF, S-S, S-S-SF, and S-S-BF). SF stands for steel fiber and BF for basalt fiber. All the beams were subjected to four-point bending test. The error bars correspond to standard deviation from three or more replicate specimens.

3.2. Post-peak response as a function of print geometry and configuration, and fiber reinforcement

Representative load-mid-point deflection responses of the beams from the four-point bending tests are shown in Figure 10. The tests were carried out until the beams failed completely, or the load in the post-peak regime dropped to 500 N, or a total test run-time of 40 min (equivalent to a mid-point deflection of 0.8 mm) from the start of the test, whichever occurred earlier. The load-deflection responses, rather than the stress-strain curves, are shown here since the beams were cut from slabs, and slight dimensional inaccuracies could be present. The load-deflection responses of the unreinforced beams are shown in Figure 10(a). All the specimens show a rather brittle behavior, as expected. However, an important observation from this figure is that, when alternate print layouts and configurations are attempted, the mid-point deflection (indicative of the strain) at the peak load increases. From approximately 0.1 mm at the peak load for a conventionally printed specimen (L-C), the mid-point deflection increases to about 0.15 mm for S-shaped conventional (S-C), and to approximately 0.12 mm for the 3-shaped layout (3-C). Staggering the layers also results in enhanced deflections at the peak load. Increase in midpoint deflection is also correlated with increased load capacity (or failure stress), as mentioned in an earlier section. The effect of fiber reinforcement on the load-deflection response of the beams printed in the staggered configuration is shown in Figure 10(b). For the same volume of fibers, the stiff steel fibers are shown to provide a considerable degree of post-peak toughness. Between the linear and S-shaped layouts for the steel fiber reinforced mixtures, the S-shaped layout shows a higher mid-point deflection at the peak load as explained earlier, but the post-peak response

at higher deflections is found to be invariant of the layout. The basalt fibers do not provide the same degree of toughness enhancement, even though the peak strength is enhanced for reasons described earlier.

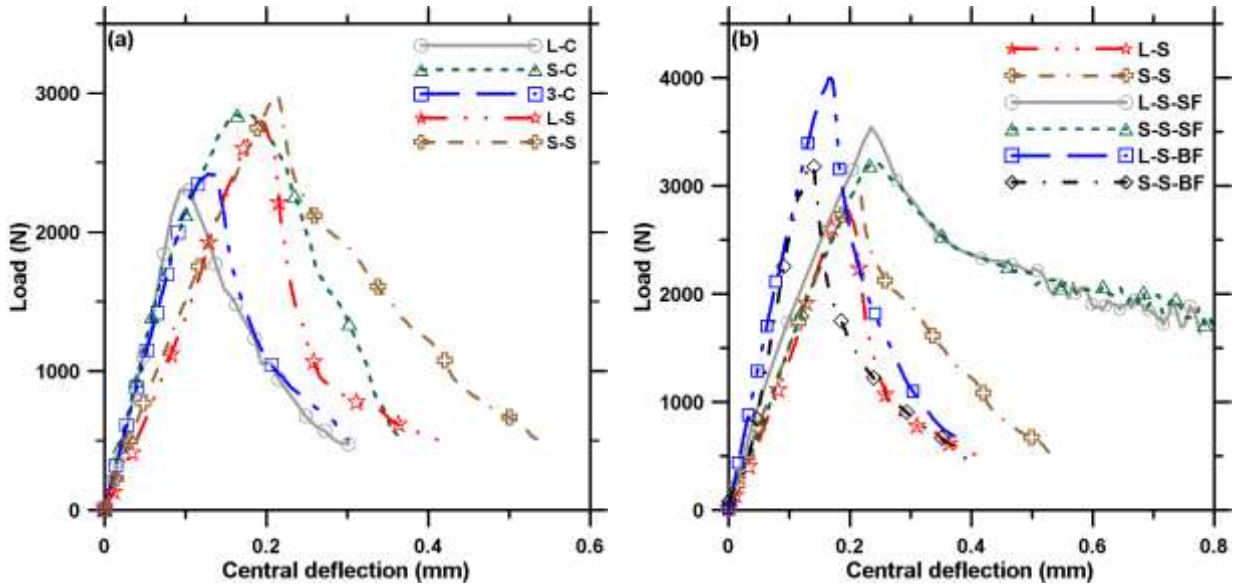

Figure 10: Load-deflection response of: (a) unreinforced beams, printed with different layouts and configurations, and (b) unreinforced and fiber-reinforced beams printed using a staggered configuration.

3.3. Layout- and configuration-induced changes in strain profiles

Digital image correlation (DIC) is used to obtain the strain profiles of the beams tested under flexure. DIC analysis of representative surface strain profiles in the middle-third portion of the beam span, under four-point bending, at or very close to the peak load are shown in Figure 11 for all the layout and fiber type combinations. The Lagrangian strain fields were extracted from the displacement fields determined from DIC. The Lagrangian strain ranges in each of the cases are also shown along with the representative images since their magnitude changes based on the chosen combination.

Figure 11(a)-(c) depict the strain fields for the conventional orientation of the L-, S-, and 3-shaped configurations. The maximum strain at failure is higher for the S-C beam, while the L-C beam has the least strain at failure. Note that both the S-C and 3-C configurations also have higher peak stresses as well, as shown in Figure 8. Since the material and printing parameters, including the layer height, are the same for all these cases, it can be concluded that the enhancement in strain at the peak load is a result of changed print layout, the effects of which has been reported earlier in the section on flexural strengths. It is important to mention here that the discussions are based on the strains observed at the peak load alone; this typically occurs at the point of crack formation or localization. Redistribution of strains occurs in the specimen when a crack forms, and thus the strains at peak stress shown here are not indicators of the average strain that will be measured across the depth or a gage length when LVDTs or strain gages are used. It is also not necessary

that the average strains follow the trends indicated by the value at peak stress. This important distinction should be considered when comparing strains determined using DIC.

When the layers are staggered (Figure 11(a) and (d) that compare L-C and L-S beams), it is noticed that there is a more than 50% enhancement in the maximum strain at the peak stress because of the staggering of alternate layers along the height of the beam. The enhancement in peak strains as a result of print layout changes (S- and 3-shapes) and staggering indicates that the failure at lower strains (a more brittle behavior) in conventional prints (straight lines, layers laid one on top of the other) is a result of combined effects of inter-filament and inter-layer defects. While changing the print layout enables curving of the filaments and thus minimizes stress concentrations, staggering of layers introduces tortuosity in the defect path (all the inter-filament joints are not on top of each other); both resulting in the specimens being able to tolerate higher maximum strains (and stresses) before failure. Figure 11(d) and (g) enable comparison between the L- and S-shaped beams where the layers are in a staggered configuration for both the beams. Here, the S-S beam shows a slightly higher maximum strain at peak stress than the L-S beam, but the effect is not as significant as that between a conventional and staggered case. This result shows that staggering of layers has a more significant effect than changing the print layout with respect to peak strains. A similar, but less conspicuous effect is noticed for the peak stresses as well.

The influence of fibers on the strains at peak stress are also shown in Figure 11(e)-(f) and (h)-(i) for the L-S and S-S beams. As discussed earlier, only the staggered configuration is shown here. Even until the peak load, the steel fiber reinforced specimens show significantly higher maximum strains, commensurate with the enhancement in peak stress. Between the L-S-SF and S-S-SF specimens, i.e., in the L- and S-shaped staggered configurations (Figure 11(e) and (h)), there is a reduction in the maximum strain for the staggered S-shaped configuration as the fibers are not oriented along the isostrain lines in the tensile region because of the curved layer layout. The steel fiber reinforced specimens demonstrate higher maximum strains as compared to the basalt fiber reinforced specimens at the peak stress as shown in Figure 11(e)-(f) and (h)-(i). The basalt fibers are more brittle than the steel fibers, have a lower stiffness, and their strain capacity is also lower (1% failure strain compared to 11% for steel fibers). As mentioned earlier, between the L- and S-shapes when layers are staggered, there is no significant difference between the peak strains for specimens reinforced with a particular fiber type, indicating that staggering creates a more dominant effect in the pre-peak (both stress and strain) mechanical response than the chosen layouts alone.

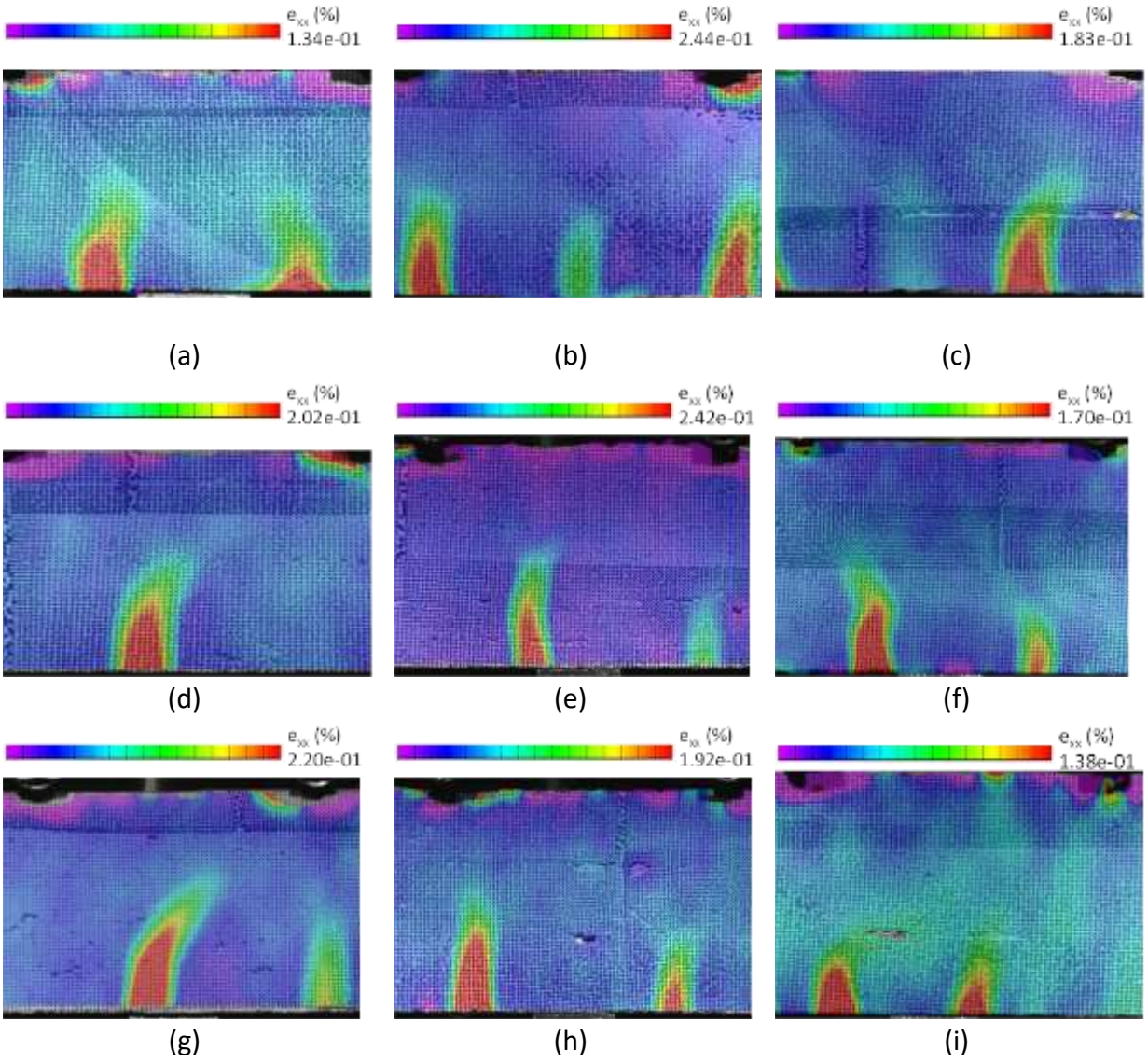

Figure 11: Lagrangian strain profiles at peak load for different layouts and configurations: (a) L-C, (b) S-C, (c) 3-C, (d) L-S, (e) L-S-SF, (f)L-S-BF, (g) S-S, (h)S-S-SF, and (i) S-S-BF.

Since the unreinforced beams do not carry significant strains after the peak load (even though changes in layout and configuration seem to define better performance than conventionally layered systems), the post-peak strain distributions in fiber-reinforced beams are only reported here. Figure 12(a)-(b) depict the strain distributions in the L-S-SF and L-S-BF beams, while Figure 12(c)-(d) show the strain distributions in the S-shaped configurations, i.e., S-S-SF and S-S-BF. Since the steel fiber reinforced beams showed a very gradual load reduction in the post-peak region because of the ductility provided by the steel fibers, the strain profiles are recorded for a mid-point deflection of 0.8 mm, when the test was ended. This corresponded to residual loads slightly higher than 50% of the peak load. The maximum strain values recorded at end of the test for both the steel fiber reinforced specimens, i.e., L-S-SF and S-S-SF (Figure 12(a) and (c) respectively) are about twice of that of the unreinforced beams. While a cursory look at the load-deflection

response (Figure 10) shows that the mid-point deflections at the end of the test are ~4 times that at the peak load, the recorded strains are ~6 times as that of the maximum strain at the peak for the corresponding specimens (shown in Figure 11(e) and (h)). This is because the post-peak maximum strains reported are at the crack tips rather than at the extreme tension fibers of the beams. As the crack initiates and surface separation occurs, the strain drops to zero, and hence a measurable strain at the crack tip where the strain is maximum, is shown. The propagation of a single crack is shown in these figures, which is the dominant crack for steel fiber reinforced specimens (note multiple locations of larger strains are seen in the strain distribution image at peak load). The volume of fibers is small enough that multiple cracking (as is noted for ultra high-performance concrete (UHPC) beams in [21], [33]) is not mobilized in these specimens. Basalt fiber reinforced beams did not have such a noticeable post-peak response as the steel fiber reinforced specimens because of the lower stiffness and ductility of basalt fibers [10], [34]. Thus, the maximum strains recorded are also lower, even though they help achieve similar or slightly higher strengths than steel fiber reinforced specimens because of reasons described earlier.

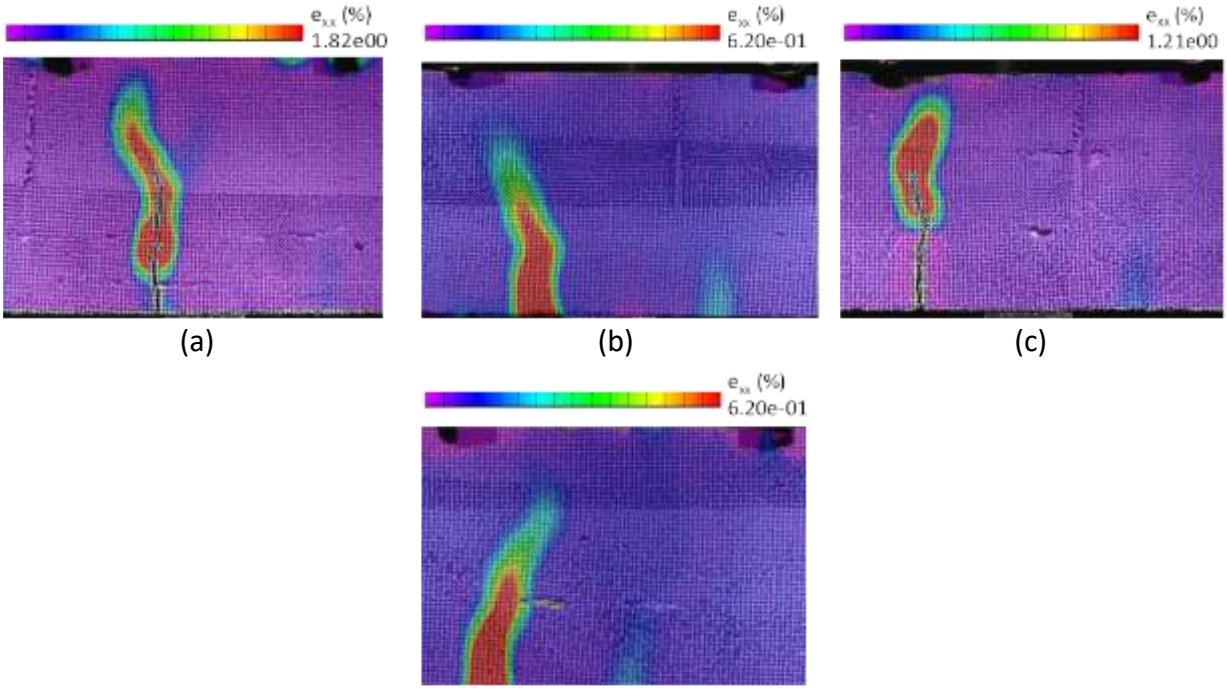

Figure 12: Lagrangian strain profile at 50% of the peak load in the post-peak region for: (a) L-S-SF, (b) L-S-BF, (c)S-S-SF, and (d) S-S-BF; Note: for L-S-SF and S-S-SF, the residual load did not drop to 50% of the peak until the end of the test (see Figure 10), and the last frame before the end of the test (mid-point deflection of 0.8 mm) is shown.

3.4. Compressive strength

As explained in a previous section, 60 mm cubes were used for compression strength testing. Since 3D printed samples are anisotropic, the compressive strength was evaluated in all the three directions as shown in Figure . At least three samples were tested on each direction and the

compressive strength results are shown in Figure 13. The results for the straight filament layout prints (L series) are shown in Figure 13(a), whereas the results for the S-shaped layouts are shown in Figure 13(b); in both the figures, two orientations (conventional and staggered) and two fiber types (steel and basalt) are also considered. As explained earlier, fiber reinforcement is used only in the staggered configuration. As has been previously reported [10], [11], [18], [35], the inherent anisotropy in compression of 3D printed components is brought out. It can be noticed that Direction-2 is the weakest among the three directions, while Directions-1 and 3 demonstrate relatively similar strengths for all the cases considered in this study. The maximum compressive strength at 28 days is almost 75 MPa for many of the cases, indicating that 3D printed mixtures with up to 30% cement replacement with limestone can attain high compressive strengths for many structural applications.

From Figure 13(a) and (b), it can be noticed that the differences in compressive strength between mixtures printed with different layouts, configurations, or fiber reinforcement types are not very significant, unlike the case for flexure reported earlier in this paper. However, anisotropy in compression is evident based on the obtained lower strength when tested in Direction-2. There are conflicting results reported in this regard. For example, it is shown in [18] that Direction-3 is the strongest and Direction-1 the weakest; however, this is likely because of the fact that only a single filament was incorporated in each layer of the cube in those tests, while the current work uses a cut portion from a printed slab, which comprises multiple filaments. On the other hand, [19] also utilizes cubes with each layer consisting of a single filament and reports that Direction-2 is usually the strongest while Direction-3 is the weakest. Similarly, another work [36] reports that Direction-1 is stronger than Direction-2. Nevertheless, as inter-filamentous joints corresponding to layers in X-Y plane (See Figure 8(a)) are locations of potential weakness, evaluating anisotropy with test specimens having multiple filaments in the same layer is important. While a typical 60 mm cube for all the different print types used in this study has the same interlayer (horizontal) joint area (of ~18,000 mm^2), a straight (linear) conventionally printed cube has ~7200 mm^2 of inter-filamentous vertical joint area compared to ~9000 mm^2 for a linear staggered print cube. Thus, the linear staggered configuration shows somewhat lower strength in compression in Direction-1 than its conventionally printed counterparts. In Directions-2 and 3, this effect is not dominant, resulting in comparable strengths for the conventional and staggered configurations. For the S-shaped prints shown in Figure 13(b), staggering slightly reduces the strength in Direction-3 for the unreinforced mixture, though it is unclear if it is just an experimental artifact. While steel fiber reinforced mixtures display comparable compressive strengths to their unreinforced counterparts with similar layer geometry and orientation, the basalt fiber reinforced mixtures show reduced compressive strengths. This is in contrast to the behavior in flexure noted earlier. It was mentioned that the scratching of the layer surface by stiff and long steel fibers leads to interlayer defects, which are detrimental in flexure, but such defects are not critical in compression. Chopped basalt fibers are generally reported to result in some enhancement in compressive strength of concrete at volume fractions comparable to those used in this work. However, it is possible that, with larger number of fibers per unit volume, basalt

fibers likely could influence the sampling volume under compression (the entire specimen volume is under compression) more than steel fibers. Here, due to: (i) fiber-matrix interface defects, and (ii) the increased number of basalt fibers reducing the packing density of the matrix [37], the compressive strength is reduced. Under flexure, the sampling volume under tension is much smaller, and hence it is feasible that there is a higher statistical possibility of encountering a larger defect in a fine fiber reinforced matrix under compression. This aspect requires further investigation, using a range of fiber volume fractions, which is beyond the scope of this work, the focus of which is the evaluation of property differences with layout, configuration, and fiber type.

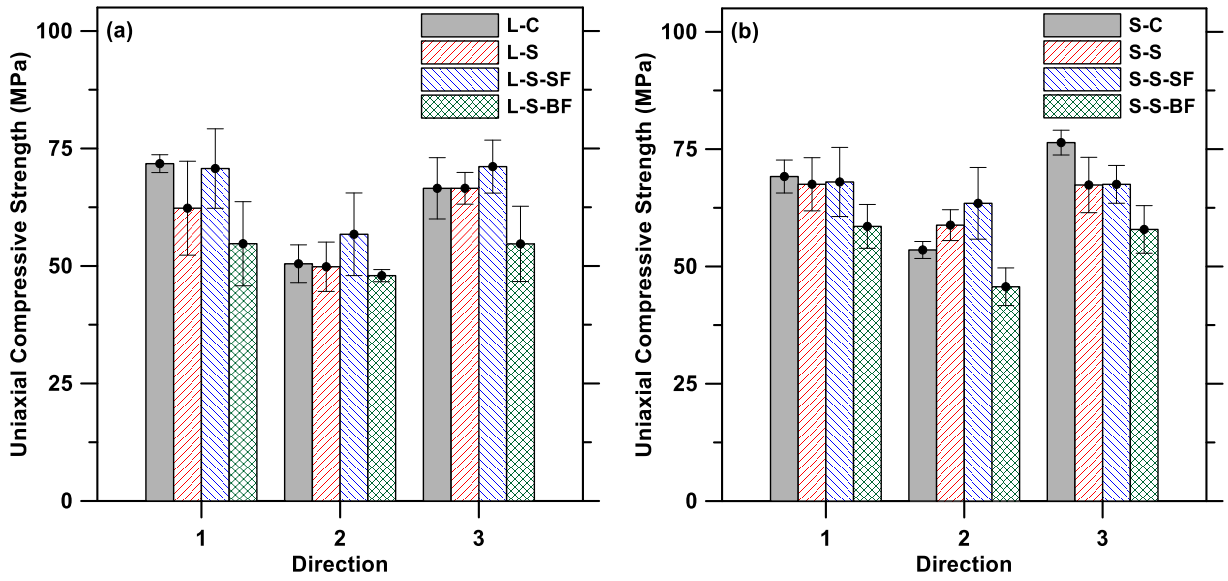

Figure 13: Uniaxial compressive strength in three orthogonal directions for (a) L-C vs L-S vs L-S-SF vs L-S-BF, and (b) S-C vs S-S vs S-S-SF vs S-S-BF.

4. Conclusions

This study has examined the influence of print geometry and configuration on the flexural and compressive response of 3D printed concrete elements. In the conventional printing approach, straight filaments are overlaid in different layers (resulting in inter-layer joints) and several such filaments are laid side-by-side to obtain desired member thicknesses (resulting in inter-filament joints). In this study, S- and 3-shaped print patterns and staggering of the layers were studied in order to reduce the impact of inter-filament joints on mechanical properties. Flexural and compressive strength tests were carried out on the specimens, along with digital image correlation (DIC) on the flexural specimens. Steel or basalt fibers were also used in some of the mixtures.

- Among the different print geometries, the S-shaped (in plan) print geometry provided flexural strengths that were 10% higher than the conventional (straight line - L) print path. Staggering the layers by half a layer width as compared to the top and bottom layers further enhanced the flexural strengths, resulting in approximately 25% enhancement in strength as compared

to the conventional print type. An increase in flexural strength by about 10-30% was observed when steel or basalt fibers were incorporated into the specimens printed in the L and S-shaped staggered layouts. The enhancement was more noticeable for the staggered linear (L-S) print type.

- Steel fibers provided enhanced flexural ductility at the same replacement volume as compared to basalt fibers, though basalt fibers provided slightly higher strengths. The fact that rigid steel fibers, which are slightly longer than the layer height scratches the layer surface, causing surface defects, could be the likely reason for the slightly lower strengths. Thus, the use of less stiff fibers is preferable when using longer fibers or when the layer height needs to be limited. Between the linear and S-shaped layouts for the steel fiber reinforced mixtures, the S-shaped layout showed a higher mid-point deflection at the peak load, indicating the efficiency of changing geometry in strain capacities as well.
- The peak strains determined using DIC were lower for the conventional prints (straight lines, layer one on top of the other), while they were higher when the print layout changed (S- and 3-shapes) or when the layers were staggered. This demonstrates that a more brittle behavior in conventional prints is a result of combined effects of inter-filament and inter-layer defects. Changes in the print layout minimizes stress concentrations while staggering of layers introduces tortuosity in the defect path, resulting in the specimens able to tolerate higher maximum strains (and stresses) before failure.
- The anisotropy effects in compression are captured in this work. Here, Direction-2 was found to be the weakest among the three directions, while Directions-1 and 3 showed similar strengths. The need to use multiple filaments in a single layer to evaluate the anisotropic behavior, since inter-filament joints within a layer are potential regions of weakness and hence a cause of anisotropy, was also brought out.

This study has shown that modifications in print geometry (shapes and orientation) as well as material characteristics (through the use of fiber reinforcement) can be used to mitigate some of the undesirable strength-related effects of inter-filament joints in layered 3D printing of concrete.

5. Acknowledgement

The authors sincerely acknowledge support from U.S. National Science Foundation (CMMI: 1727445; OISE: 2020095) towards this this project. The contents of this paper reflect the views of the authors who are responsible for the facts and accuracy of the data presented herein, and do not necessarily reflect the views and policies of NSF, nor do the contents constitute a standard, specification, or a regulation. The authors acknowledge the support from Salt River Materials Group, Omya, BASF, Bekaert, and Rock fiber for donating the materials. We acknowledge the use of 3D printing and material characterization facilities within Laboratory for the Science of Sustainable Infrastructural Materials (LS-SIM) at Arizona State University.

References

[1] Y. Chen, F. Veer, and O. Çopuro, “A critical review of 3D concrete printing as a low CO2 concrete approach,” p. 29.

[2] G. Vantyghem, W. De Corte, E. Shakour, and O. Amir, “3D printing of a post-tensioned concrete girder designed by topology optimization,” *Automation in Construction*, vol. 112, p. 103084, Apr. 2020, doi: 10.1016/j.autcon.2020.103084.

[3] P. Wu, J. Wang, and X. Wang, “A critical review of the use of 3-D printing in the construction industry,” *Automation in Construction*, vol. 68, pp. 21–31, Aug. 2016, doi: 10.1016/j.autcon.2016.04.005.

[4] B. Nematollahi, M. Xia, and J. Sanjayan, *Current Progress of 3D Concrete Printing Technologies*. 2017. doi: 10.22260/ISARC2017/0035.

[5] C. Holt, L. Edwards, L. Keyte, F. Moghaddam, and B. Townsend, “Chapter 17 - Construction 3D Printing,” in *3D Concrete Printing Technology*, J. G. Sanjayan, A. Nazari, and B. Nematollahi, Eds. Butterworth-Heinemann, 2019, pp. 349–370. doi: 10.1016/B978-0-12-815481-6.00017-8.

[6] S. Z. Jones, D. P. Bentz, N. S. Martys, W. L. George, and A. Thomas, “Rheological Control of 3D Printable Cement Paste and Mortars,” in *First RILEM International Conference on Concrete and Digital Fabrication – Digital Concrete 2018*, Cham, 2019, pp. 70–80. doi: 10.1007/978-3-319-99519-9_7.

[7] Y. Chen *et al.*, “Improving printability of limestone-calcined clay-based cementitious materials by using viscosity-modifying admixture,” *Cement and Concrete Research*, vol. 132, p. 106040, Jun. 2020, doi: 10.1016/j.cemconres.2020.106040.

[8] C. Eugenin, I. Navarrete, W. Brevis, and M. Lopez, “Air Bubbles as an Admixture for Printable Concrete: A Review of the Rheological Effect of Entrained Air,” *3D Printing and Additive Manufacturing*, Apr. 2021, doi: 10.1089/3dp.2020.0302.

[9] G. Vantyghem, V. Boel, W. De Corte, and M. Steeman, “Compliance, Stress-Based and Multi-physics Topology Optimization for 3D-Printed Concrete Structures,” in *First RILEM International Conference on Concrete and Digital Fabrication – Digital Concrete 2018*, Cham, 2019, pp. 323–332. doi: 10.1007/978-3-319-99519-9_30.

[10] S. Kristombu Baduge *et al.*, “Improving performance of additive manufactured (3D printed) concrete: A review on material mix design, processing, interlayer bonding, and reinforcing methods,” *Structures*, vol. 29, pp. 1597–1609, Feb. 2021, doi: 10.1016/j.istruc.2020.12.061.

[11] R. J. M. Wolfs, F. P. Bos, and T. A. M. Salet, “Hardened properties of 3D printed concrete: The influence of process parameters on interlayer adhesion,” *Cement and Concrete Research*, vol. 119, pp. 132–140, May 2019, doi: 10.1016/j.cemconres.2019.02.017.

[12] A. S. Alchaar and A. K. Al-Tamimi, “Mechanical properties of 3D printed concrete in hot temperatures,” *Construction and Building Materials*, vol. 266, p. 120991, Jan. 2021, doi: 10.1016/j.conbuildmat.2020.120991.

[13] A. Perrot, D. Rangeard, and A. Pierre, “Structural built-up of cement-based materials used for 3D-printing extrusion techniques,” *Mater Struct*, vol. 49, no. 4, pp. 1213–1220, Apr. 2016, doi: 10.1617/s11527-015-0571-0.

[14] N. Roussel, “Rheological requirements for printable concretes,” *Cement and Concrete Research*, vol. 112, pp. 76–85, Oct. 2018, doi: 10.1016/j.cemconres.2018.04.005.

[15] B. Zareiyan and B. Khoshnevis, “Effects of interlocking on interlayer adhesion and strength of structures in 3D printing of concrete,” *Automation in Construction*, vol. 83, pp. 212–221, Nov. 2017, doi: 10.1016/j.autcon.2017.08.019.

[16] N. M. Salman, G. Ma, N. Ijaz, and L. Wang, “Weak inter-layer bonding in extrusion 3D concrete printing: a comparative analysis of mitigation techniques,” *IOP Conf. Ser.: Mater. Sci. Eng.*, vol. 1028, p. 012003, Jan. 2021, doi: 10.1088/1757-899X/1028/1/012003.

[17] E. Keita, H. Bessaies-Bey, W. Zuo, P. Belin, and N. Roussel, “Weak bond strength between successive layers in extrusion-based additive manufacturing: measurement and physical origin,” *Cement and Concrete Research*, vol. 123, p. 105787, Sep. 2019, doi: 10.1016/j.cemconres.2019.105787.

[18] B. Panda, S. Chandra Paul, and M. Jen Tan, “Anisotropic mechanical performance of 3D printed fiber reinforced sustainable construction material,” *Materials Letters*, vol. 209, pp. 146–149, Dec. 2017, doi: 10.1016/j.matlet.2017.07.123.

[19] J. Ye, C. Cui, J. Yu, K. Yu, and F. Dong, “Effect of polyethylene fiber content on workability and mechanical-anisotropic properties of 3D printed ultra-high ductile concrete,” *Construction and Building Materials*, vol. 281, p. 122586, Apr. 2021, doi: 10.1016/j.conbuildmat.2021.122586.

[20] R. Yu, P. Spiesz, and H. J. H. Brouwers, “Development of an eco-friendly Ultra-High Performance Concrete (UHPC) with efficient cement and mineral admixtures uses,” *Cement and Concrete Composites*, vol. 55, pp. 383–394, Jan. 2015, doi: 10.1016/j.cemconcomp.2014.09.024.

[21] A. Arora, Y. Yao, B. Mobasher, and N. Neithalath, “Fundamental insights into the compressive and flexural response of binder- and aggregate-optimized ultra-high performance concrete (UHPC),” *Cement and Concrete Composites*, vol. 98, pp. 1–13, Apr. 2019, doi: 10.1016/j.cemconcomp.2019.01.015.

[22] S. A. O. Nair, H. Alghamdi, A. Arora, I. Mehdipour, G. Sant, and N. Neithalath, “Linking fresh paste microstructure, rheology and extrusion characteristics of cementitious binders for 3D printing,” *Journal of the American Ceramic Society*, vol. 102, no. 7, pp. 3951–3964, 2019, doi: 10.1111/jace.16305.

[23] S. A. O. Nair, A. Tripathi, and N. Neithalath, “Examining layer height effects on the flexural and fracture response of plain and fiber-reinforced 3D-printed beams,” *Cement and Concrete Composites*, vol. 124, p. 104254, Nov. 2021, doi: 10.1016/j.cemconcomp.2021.104254.

[24] ASTM International, “C78/C78M-18 Standard test method for flexural strength of concrete (using simple beam with third-point loading),” ASTM International, West Conshohocken, PA, 2018. doi: 10.1520/C0078_C0078M-18.

[25] S. Das, A. Kizilkanat, and N. Neithalath, “Crack propagation and strain localization in metallic particulate-reinforced cementitious mortars,” *Materials & Design*, vol. 79, pp. 15–25, Aug. 2015, doi: 10.1016/j.matdes.2015.04.038.

[26] D. Zhang, C. D. Eggleton, and D. D. Arola, “Evaluating the mechanical behavior of arterial tissue using digital image correlation,” p. 8.

[27] I. Marković, *High-performance Hybrid-fibre Concrete: Development and Utilisation*. IOS Press, 2006.

[28] F. Bester, M. van den Heever, J. Kruger, S. Cho, and G. van Zijl, “Steel Fiber Links in 3D Printed Concrete,” in *Second RILEM International Conference on Concrete and Digital Fabrication*, Cham, 2020, pp. 398–406. doi: 10.1007/978-3-030-49916-7_41.

[29] A. R. Arunothayan, B. Nematollahi, J. Sanjayan, R. Ranade, S. H. Bong, and K. Khayat, “Quantitative Evaluation of Orientation of Steel Fibers in 3D-Printed Ultra-High Performance Concrete,” in *Second RILEM International Conference on Concrete and Digital Fabrication*, Cham, 2020, pp. 389–397. doi: 10.1007/978-3-030-49916-7_40.

[30] F. P. Bos, E. Bosco, and T. A. M. Salet, “Ductility of 3D printed concrete reinforced with short straight steel fibers,” *Virtual and Physical Prototyping*, vol. 14, no. 2, pp. 160–174, Apr. 2019, doi: 10.1080/17452759.2018.1548069.

[31] B. Nematollahi *et al.*, “Effect of Polypropylene Fibre Addition on Properties of Geopolymers Made by 3D Printing for Digital Construction,” *Materials*, vol. 11, no. 12, Art. no. 12, Dec. 2018, doi: 10.3390/ma11122352.

[32] M. Hambach, M. Rutzen, and D. Volkmer, “Chapter 5 - Properties of 3D-Printed Fiber-Reinforced Portland Cement Paste,” in *3D Concrete Printing Technology*, J. G. Sanjayan, A. Nazari, and B. Nematollahi, Eds. Butterworth-Heinemann, 2019, pp. 73–113. doi: 10.1016/B978-0-12-815481-6.00005-1.

[33] B. Mobasher, A. Li, Y. Yao, A. Arora, and N. Neithalath, “Characterization of toughening mechanisms in UHPC through image correlation and inverse analysis of flexural results,” *Cement and Concrete Composites*, vol. 122, p. 104157, Sep. 2021, doi: 10.1016/j.cemconcomp.2021.104157.

[34] J. Sim, C. Park, and D. Y. Moon, “Characteristics of basalt fiber as a strengthening material for concrete structures,” *Composites Part B: Engineering*, vol. 36, no. 6, pp. 504–512, Jan. 2005, doi: 10.1016/j.compositesb.2005.02.002.

[35] L. Pham, G. Lu, and P. Tran, “Influences of Printing Pattern on Mechanical Performance of Three-Dimensional-Printed Fiber-Reinforced Concrete,” *3D Printing and Additive Manufacturing*, p. 3dp.2020.0172, Dec. 2020, doi: 10.1089/3dp.2020.0172.

[36] M. van den Heever, F. Bester, J. Kruger, and G. van Zijl, “Mechanical characterisation for numerical simulation of extrusion-based 3D concrete printing,” *Journal of Building Engineering*, vol. 44, p. 102944, Dec. 2021, doi: 10.1016/j.jobe.2021.102944.

[37] L. G. Li, H. X. Zhuo, J. Zhu, and A. K. H. Kwan, “Packing density of mortar containing polypropylene, carbon or basalt fibres under dry and wet conditions,” *Powder Technology*, vol. 342, pp. 433–440, Jan. 2019, doi: 10.1016/j.powtec.2018.10.005.